Atomic-scale simulations of reactive oxygen plasma species interacting with bacterial cell walls

2012 New J. Phys. 14 093043

(http://iopscience.iop.org/1367-2630/14/9/093043)

New Journal of Physics
The open-access journal for physics

Atomic-scale simulations of reactive oxygen plasma species interacting with bacterial cell walls

M Yusupov[1,3], E C Neyts[1], U Khalilov[1], R Snoeckx[1], A C T van Duin[2] and A Bogaerts[1]

[1] Research Group PLASMANT, Department of Chemistry, University of Antwerp, Universiteitsplein 1, 2610 Antwerp, Belgium
[2] Department of Mechanical and Nuclear Engineering, Penn State University, University Park, PA 16802, USA
E-mail: maksudbek.yusupov@ua.ac.be

New Journal of Physics **14** (2012) 093043 (18pp)
Received 15 June 2012
Published 26 September 2012
Online at http://www.njp.org/
doi:10.1088/1367-2630/14/9/093043

Abstract. In recent years there has been growing interest in the use of low-temperature atmospheric pressure plasmas for biomedical applications. Currently, however, there is very little fundamental knowledge regarding the relevant interaction mechanisms of plasma species with living cells. In this paper, we investigate the interaction of important plasma species, such as O_3, O_2 and O atoms, with bacterial peptidoglycan (or murein) by means of reactive molecular dynamics simulations. Specifically, we use the peptidoglycan structure to model the gram-positive bacterium *Staphylococcus aureus* murein. Peptidoglycan is the outer protective barrier in bacteria and can therefore interact directly with plasma species. Our results demonstrate that among the species mentioned above, O_3 molecules and especially O atoms can break important bonds of the peptidoglycan structure (i.e. C–O, C–N and C–C bonds), which subsequently leads to the destruction of the bacterial cell wall. This study is important for gaining a fundamental insight into the chemical damaging mechanisms of the bacterial peptidoglycan structure on the atomic scale.

[3] Author to whom any correspondence should be addressed.

Contents

1. Introduction

Plasma medicine and plasma's biomedical applications are attracting rapidly increasing levels of interest in plasma research [1, 2]. The fields of application include plasma-based bio-decontamination, disinfection and even tissue regeneration [3]. For this and other biomedical purposes, low-temperature atmospheric pressure plasma (LTAPP) sources, such as resistive barrier discharges [4], dielectric barrier discharges (e.g. [3, 5–7]), plasma jets (e.g. [8]) or plasma needles (e.g. [9, 10]) have been developed.

Currently, one of the main applications of LTAPP sources is the sterilization of medical tools, i.e., the treatment of heat-sensitive materials or disinfection from both gram-negative and gram-positive bacteria (see e.g. [4, 6, 10–15]). Many experimental studies have been performed on the decontamination of bacteria by altering the external plasma process parameters (e.g. gas mixture composition, driving frequency and voltage). However, gaining control over the processes occurring in the plasma itself and especially in the plasma region in contact with the bio-organism still remains a challenge. Solving this issue solely by means of experiments is extremely difficult. Indeed, even simple plasma characteristics such as temperature and density cannot be measured easily with common measuring tools such as probes, due to the small scale of LTAPPs. Even if such measurements can be carried out, they lead to possible disturbances of the plasma from the measuring tool [16]. On the other hand, non-invasive methods (such as optical emission spectroscopy) can be used instead, in order to measure plasma characteristics (e.g. the electron density, see [17]). However, these methods are limited in the information they can provide and cannot give useful information, especially regarding the processes occurring in the contact region between the plasma and the bio-organism.

Computer simulations, however, are ideally suited to tackle these issues. Indeed, plasma simulations and simulations of plasma–surface interactions can provide fundamental information about the processes occurring in the plasma and at the surface of living cells. However, until now very limited effort has been spent on modeling the plasma itself and in particular on its interaction with living organisms, such as bacteria [16]. Moreover, simulating the interaction of plasma with bacteria is very difficult compared to modeling solid

state materials. However, if a proper interatomic potential can be constructed for accurately describing all relevant interatomic interactions, molecular dynamics (MD) simulations can provide atomic scale insights into them.

Based on these considerations, we investigate the interaction of plasma species with bacterial peptidoglycan (PG), as a model system for plasma–bacteria interactions. For this purpose, reactive MD simulations based on the reactive force field (ReaxFF) potential are carried out [18], using the ReaxFF glycine-force field, as developed by Rahaman *et al* [19]. The plasma species under study are O_2 and O_3 molecules, as well as O atoms, which were previously identified as being biomedically important (see [11, 20–24]). In this work, we investigate the interaction of the above-mentioned species with PG, which is the outer part of the cell wall of gram-positive bacteria such as *Staphylococcus aureus*.

It should be mentioned that our simulations are performed under 'perfect' (or 'optimized') conditions. In reality, there might be many interactions between plasma species and liquids surrounding the bacteria—e.g. skin, wounds and other biological conditions. However, in this paper we do not take this into account. Our next study will, however, be devoted to the interaction of plasma species with PG surrounded with water molecules. Indeed, the moist environment could prevent the PG destruction in reality, since oxygen species (O, O_2 and O_3) might be less exposed to the PG in the bacterial cell wall. On the other hand, it is known that under some conditions, the plasma jet can blow away (part of) the liquid film [25]. Thus, the present simulations provide detailed insights into the mechanisms of bacterial cell wall damage by plasma species when the liquid film is not present or is blown away, or when it is of little importance.

More information about the PG structure and an overview of the computational details are presented in sections 2 and 3, respectively. The results are discussed in section 4, and finally the conclusion is given in section 5.

2. Structure of the peptidoglycan

PG, also known as murein, is an important component of the bacterial cell wall. It is found on the outside of almost all bacterial membranes [26–28]. It forms a mesh-like layer composing the cell wall and serves as a protective barrier in bacteria. The PG layer is substantially thicker in gram-positive bacteria than in gram-negative bacteria. For instance, in the gram-positive bacterium *S. aureus*, the PG structure is typically 20–30 nm thick, whereas in a gram-negative bacterium, such as *Escherichia coli*, it is only 6–7 nm thick [29–31].

As mentioned above, in this paper we consider the interaction of plasma species with the gram-positive bacterium *S. aureus* PG. Its chemical structure can be found in [31–33]. A schematic picture of the PG structure is presented in figure 1. It is assembled from repeating units consisting of a disaccharide, a stem and a bridge. The disaccharide is composed of β(1–4) linked *N*-acetylglucosamine and *N*-acetylmuramic acid (GlcNAc-MurNAc), the stem is the pentapeptide L-alanine-D-*iso*-glutamine-L-lysine-D-alanine-D-alanine (L-Ala_1-D-*iso*-Gln_2-L-Lys_3-D-Ala_4-D-Ala_5), and the bridge is a pentaglycine (Gly_1–Gly_2–Gly_3–Gly_4–Gly_5) interpeptide. The pentaglycine bridge, branching off the ε-amino group of the L-Lys of the stem peptide, connects one PG chain to the D-Ala_4 of a neighboring chain (figure 1). It is important to note that this composition is often found in nascent PG, whereas the last (fifth) D-Ala_5 residue is lost in the mature macromolecule [28]. Hence, in this paper we assume a tetrapeptide stem instead of a pentapeptide stem (see figure 1).

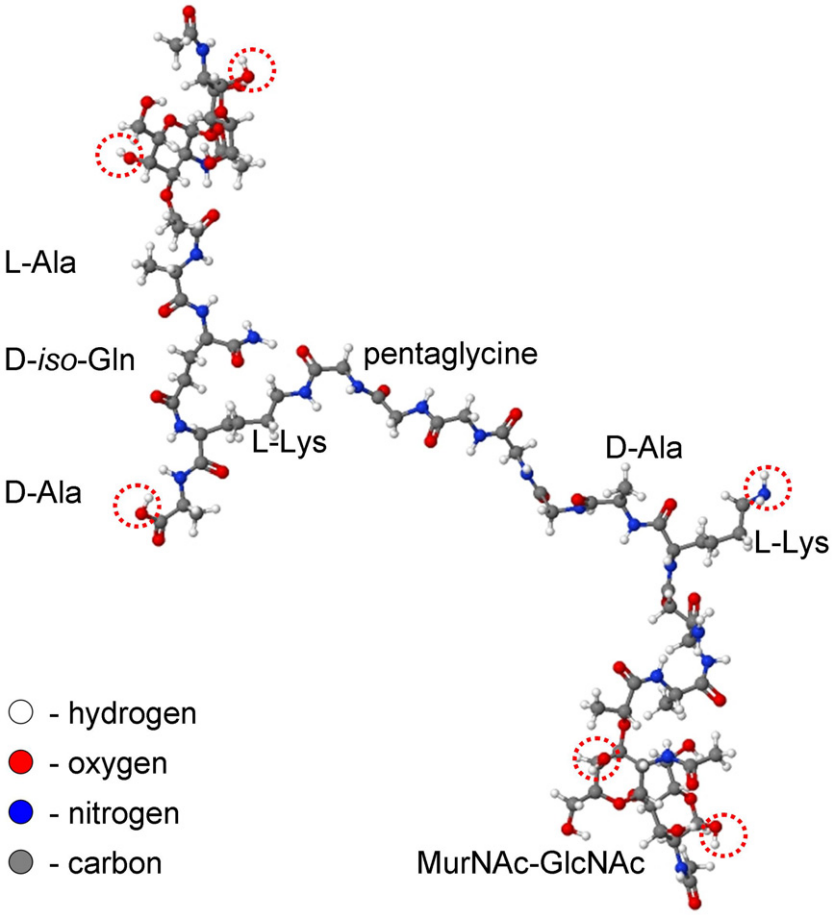

Figure 1. Schematic representation of the PG structure. Fixed atoms are indicated by red dashed circles. The color legend also applies to the other similar figures below.

Unfortunately, the exact three-dimensional structure (or tertiary structure) of the PG is still unclear and remains elusive, although many experimental investigations have been performed to define the chemical structure and to study the physical properties of the PG. One of the reasons for this is that it is not possible to distinguish the strands and peptides with conventional electron microscopy due to the similarity in dimensions of these structures and the occurring artifacts of this technique [29, 34]. However, various experimental studies have partially characterized the PG structure (see e.g. [32]). Moreover, based on these experimental studies, several models have been proposed for the three-dimensional structure of the PG, such as the vertical scaffold and the horizontal layered models [28–30, 34–36]. However, these models can explain only certain properties of the PG.

In our simulations, we model the PG structure as consisting of only two disaccharides with tetrapeptide stems (see figure 1, left and right sides), connected with one pentaglycine interpeptide (see figure 1, center). Note that with this construction we are able to take into account all possible atomic bonds in the PG structure.

3. Computational details

3.1. Interatomic potential

In an MD simulation, the trajectories of all atoms in the system are calculated by integrating the equations of motion. Forces on the atoms are derived from the ReaxFF potential [18]. This force field has now been successfully applied to describe nearly half of the periodic table of the elements and their compounds, including hydrocarbons [18, 37], metals and metal-catalyzed reactions [38, 39], metal oxides [40], metal hydrides [41] and silicon and silicon dioxide [42–44]. Recently, it has also been used for organic molecules, such as glycine [19, 45], as well as for complex molecules, such as DNA [46]. The ReaxFF parameters are optimized to obtain good general agreement with quantum mechanical calculations for reaction energies, barriers and structures (in that order of importance).

The ReaxFF potential uses the bond order/bond distance relationship formally introduced by Abell [47]. The total system energy is the sum of several partial energy terms that include lone pairs, undercoordination, overcoordination, valence and torsion angles, conjugation and hydrogen bonding. Moreover, non-bonded interactions, namely Coulomb and van der Waals energy terms, are also taken into account. These interactions are calculated between every pair of atoms, such that the ReaxFF potential is capable of describing not only covalent bonds, but also ionic bonds and the whole range of intermediate interactions. The electronegativity equalization method [48, 49] is used to calculate charge distributions based on geometry and connectivity. A detailed description of the force field parameters used in this study can be found elsewhere [19].

3.2. Simulation method

In our simulations, the PG structure is placed in a box with dimensions $\sim$75 Å $\times$ 88 Å $\times$ 51 Å. Periodic boundary conditions are not applied to any plane as no infinite surface is needed in the simulations. However, a few atoms in the structure are fixed to keep the structure from drifting. The fixed atoms are chosen such that they are positioned at the periodically repeating parts of the PG structure, i.e. O and H atoms in D-Ala_4, MurNAc and GlcNAc, as well as two H atoms in L-Lys (see figure 1, red dashed circles).

Prior to the particle impacts, the structure is equilibrated at room temperature (i.e., 300 K) as follows. First, the structure is thermalized in the isothermal–isobaric ensemble (i.e., NPT dynamics) for 100 ps to equilibrate the temperature of the system and to obtain a structure at zero stress. The obtained structure is subsequently equilibrated in the NVT ensemble using the Berendsen heat bath [50] for 40 ps. Finally, the resulting structure is relaxed in the microcanonical ensemble (i.e., NVE dynamics) for 20 ps. The temperature relaxation constant is set to 0.1 ps in all temperature controlled simulations, i.e. during the thermalization, as well as during the particle impact simulations. In all simulations, we used a time step of 0.1 fs.

In all simulations, the impacts of the plasma species are performed as follows. Ten incident particles (e.g. ten O_3 molecules) are randomly positioned at a minimum distance of 10 Å around the PG structure and also from each other. This distance ensures that there is initially no interaction between the plasma species and the PG structure due to the long distance interactions (i.e. Coulomb and van der Waals interactions). The initial energy of impinging plasma species corresponds to room temperature and their velocity directions are chosen randomly. To study all possible damaging mechanisms of the PG and to obtain statistically valid results for

bond-breaking processes, we performed 50 runs for each plasma species (i.e. for O_2, O_3, as well as for the O atoms). Every simulation trajectory lasts 300 ps, corresponding to 3×10^6 iterations. This time is long enough to obtain a chemically destroyed PG structure, at least if a critical bond in the structure is broken (see below). Thus, at the end of the simulation all plasma species interacted with the structure, possibly resulting in the breaking of various bonds as described below in section 4.

4. Results and discussion

It is clear from figure 1 that the most important bonds in the PG structure are C–C, C–N and C–O. As far as the structural integrity of the PG is concerned, the C–O bonds are of importance only in disaccharides (i.e. in MurNAc–GlcNAc, see figure 1). If these C–O bonds or any of the C–C or C–N bonds break, this will lead to the destruction of the PG. Note that there are also C–O bonds in other parts of the PG, but we do not take these into account as they are less important in damaging the PG structure.

It should also be mentioned that there are no bond cleavage events observed in the case of O_2 impacts. These molecules are found to have only weak attractive non-bonded interactions with the PG structure. Therefore, we do not consider O_2 molecules in our further investigation. In the following studies, examples of the bond-breaking mechanisms will only be shown for oxygen atoms, though similar mechanisms have also been observed for O_3 molecules. Note that in the case of O_3, the first reaction to occur is invariably with hydrogen from the PG, resulting in the formation of an O_2 molecule and an OH radical.

4.1. Dissociation of C–N bonds

One of the cleavage mechanisms of C–N bonds is presented in figure 2, where D-Ala, connected to the pentaglycine bridge, is being broken by an impinging oxygen atom (see figure 1, right-hand side). It is clear from figure 2(a) that oxygen (encircled by the red dashed line) is reacting with hydrogen initially bound with carbon, i.e. a hydrogen-abstraction reaction is taking place. Note that there is another oxygen (shown by the dashed green circle) that has already abstracted a hydrogen atom from another carbon atom. As we concentrate on the breaking of C–N bonds in this section, an explanation for this process will be given later. As shown in figure 2(b), the distance between the C–C bonds starts to decrease after the hydrogen-abstraction reaction (cf bond distances in figures 2(a) and (b)). Because of the hydrogen abstraction, a primary alkyl radical is generated in D-Ala. Since this radical is not stable [51], a double C–C bond is created by homolytic cleavage of the C–N bond, with the formation of a resonance-stabilized amide radical (see figure 2(c)). Note that the resonance-stabilized amide radical is more stable than the primary radical, which could therefore be the driving force for the C–N bond-breaking process. It should also be noted that also a secondary alkyl radical is created after the hydrogen abstraction (see dashed green circle in figure 2(a)). Since secondary alkyl radicals are more stable than primary alkyl radicals, no bond breaking takes place in this case.

After dissociation of the C–N bond, the two carbon atoms form a double bond (see figure 2(c)). The average C–C bond length does not change further until the end of the simulation and is found to be about 1.33 Å, i.e. a typical value for the bond length of a double C–C bond [51], as shown in figure 3 (see red dashed line).

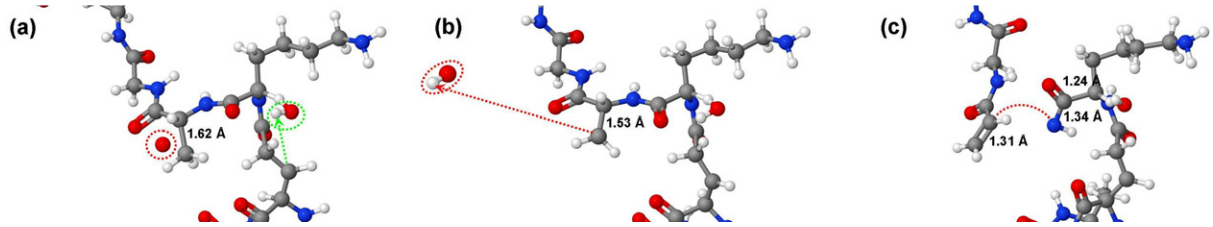

Figure 2. Snapshots from MD simulations, showing the interaction of an oxygen atom with D-Ala, leading to the cleavage of a C–N bond. (a) Oxygen, shown in red dashed circle, reacts with hydrogen ($t = 15.6$ ps). (b) Hydrogen abstraction takes place and results in a decrease in the C–C bond length ($t = 16.2$ ps). (c) Cleavage of the C–N bond (indicated by the red dashed line) and creation of the double C–C bond ($t = 30.6$ ps). Note that there is another oxygen atom (shown by the dashed green circle, see (a)) that abstracts a hydrogen atom from another carbon atom, resulting in the formation of a secondary alkyl radical.

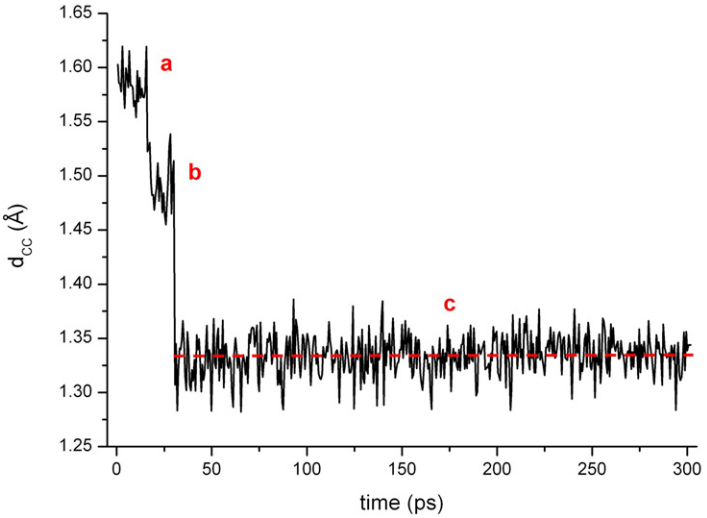

Figure 3. Time evolution of C–C bond length. The **a**, **b** and **c** labels correspond to (a), (b) and (c) in figure 2, respectively. After 30.6 ps, the average distance between the carbon atoms remains constant until the end of the simulation. The average C–C bond length is about 1.33 Å, which is typical for a double C–C bond (see red dashed line).

In figure 4 the time evolution of the average number of C–N bonds is shown. Note that the average number of C–N, C–C and C–O bonds is calculated from 50 independent runs for each incident species. It is clear from the figure that the average number of C–N bonds decreases during the simulation, i.e., the plasma species effectively break the C–N bonds in the PG structure. It is also obvious from figure 4 that most of the C–N bonds break due to oxygen impacts, rather than due to O_3 molecules. When oxygen is used as the impacting species, dissociation of C–N bonds is observed in 26% of the simulations cases. When O_3 is used, on the other hand, this value decreases to 8% (see table 1). Moreover, it is also observed that most of the C–N bond dissociations occur only in alanines. In the case of impacting O atoms, for instance, almost 80% of the C–N bond dissociations occur in alanines. Note, however, that the

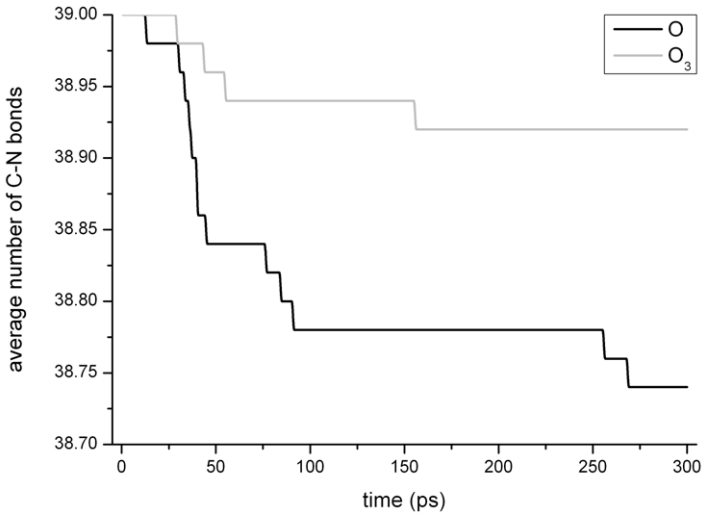

Figure 4. Time evolution of the average number of C–N bonds upon the impingement of O atoms and O_3 molecules. The value of the average number is calculated from 50 independent simulations for each incident species.

Table 1. Fraction of dissociation events of important bonds (i.e. C–N, C–O and C–C bonds) upon impact of O atoms or O_3 molecules. The values are calculated from 50 independent simulations for each incident species.

Incident plasma species	C–N bond-breaking events (%)	C–O bond-breaking events (%)	C–C bond-breaking events (%)
O atoms	26	78	38
O_3 molecules	8	56	26

dissociation of C–N bonds occurs only due to the hydrogen abstraction from a methyl group in the alanines (see below).

The calculated bond length distribution of the carbon atoms is shown in figure 5 for different simulation times. At the beginning of the simulation ($t = 0$ ps), there is only one peak centered at ~1.56 Å, indicative of single C–C bonds [51]. After 150 ps, the amplitude of this peak decreases and a new maximum appears at ~1.34 Å, indicating the presence of double C–C bonds. In the subsequent 150 ps, this maximum continues to increase slightly, indicating that the number of double C–C bonds is increasing. Note that the formation of double C–C bonds can only be due to hydrogen abstraction by plasma species. As demonstrated above, this can lead to the breaking of neighboring bonds in some cases (e.g. C–N bonds in alanines, see above).

It should also be mentioned that the breaking of C–N bonds in alanines depends on the position of the hydrogen abstraction taking place in the alanine. Our observations show that if the hydrogen abstraction primarily takes place in the methyl part of the alanine, this eventually leads to the formation of a double C–C bond and the destruction of the neighboring C–N bond (see e.g. figure 2). On the other hand, if the hydrogen abstraction primarily takes place in the central part of the alanine, it cannot lead to a cleavage of the C–N bond, even if a double C–C bond is formed. For instance, it is obvious from figure 6 that after two hydrogen-abstraction

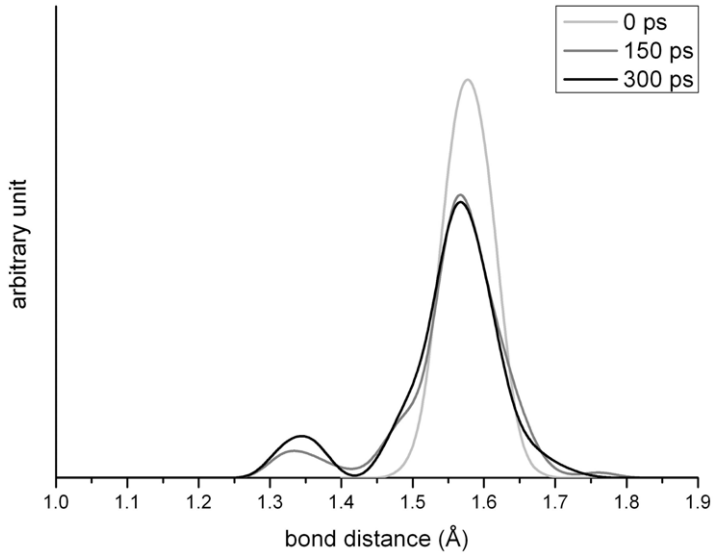

Figure 5. Bond length distribution of carbon atoms after different simulation times, i.e. after 0, 150 and 300 ps. The peaks around 1.56 and 1.34 Å correspond to single and double C–C bonds, respectively.

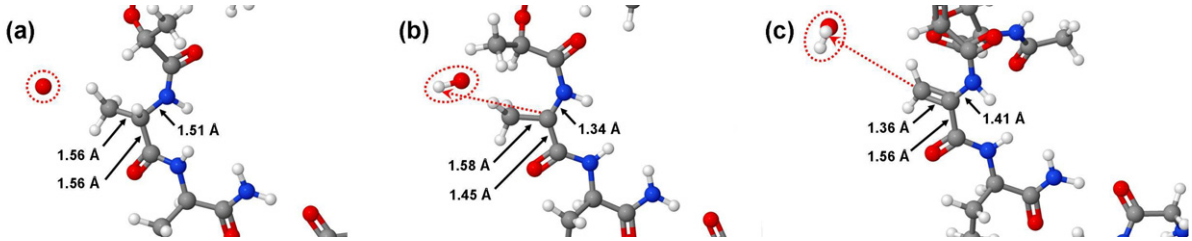

Figure 6. Snapshots from MD simulations, showing the interaction of an oxygen atom with L-Ala, leading to the formation of a double C–C bond. (a) Oxygen, shown in red dashed circle, reacts with hydrogen positioned at the centre of L-Ala ($t = 9.6$ ps). (b) Hydrogen abstraction takes place ($t = 19.2$ ps). (c) Second hydrogen abstraction takes place in methyl residue of L-Ala and double C–C bond is formed ($t = 45$ ps).

reactions in L-Ala (see figure 1, left side of the PG), a double C–C bond is created without any bond breakage (see figure 6(c)). Indeed, the first hydrogen abstraction occurs in the central part of the alanine (see figure 6(b)) with the formation of a carbon radical. This radical is stabilized by its amide neighbors due to electron delocalization effects [52] and is therefore more stable than the primary radical mentioned above (see figure 2(a)). Hence, after the second hydrogen abstraction, a primary radical is also created and these two radicals subsequently form a stable double C–C bond (see figure 6(c)).

Note that breaking of C–N bonds is also observed in other parts of the PG. Our calculations show that the mechanism of the C–N bond dissociation in these parts is similar to the cleavage mechanism in alanines as described above, i.e. it occurs due to hydrogen abstraction and subsequent formation of double C–C bonds. However, no C–N bond-breaking events were observed in the pentaglycine interpeptide, even when hydrogen abstraction took place. This

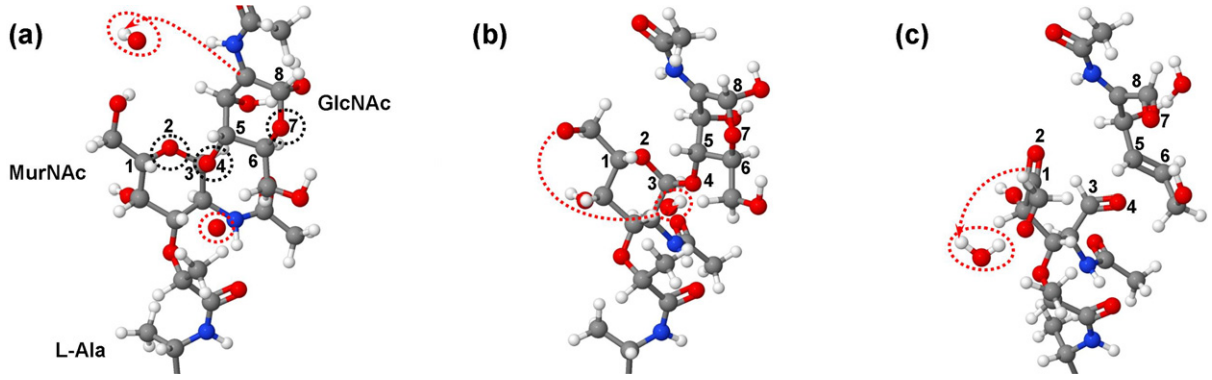

Figure 7. Snapshots from MD simulations, showing the consecutive breaking mechanisms of three important ether C–O bonds (see black dashed circles) upon oxygen atom impact. (a) First oxygen atom abstracts the hydrogen from GlcNAc (see first red dashed circle, $t = 16.8$ ps). (b) Another hydrogen is abstracted from MurNAc by a second oxygen atom, resulting in the formation of an OH radical (see red dashed circle, $t = 45$ ps). (c) The OH radical abstracts another hydrogen atom, which is connected to C_1 (cf C_1 from (b)), and a water molecule is created ($t = 45.6$ ps). Subsequently, some double C–O and C–C bonds are formed, which lead to breaking of the C–O ether bonds (cf the bonds between numbered atoms from (b) and (c), and see text for a detailed description of the mechanism).

is probably due to the resonance-stabilized structure of pentaglycine. We should also mention that the examples of the C–N bond-breaking mechanisms were demonstrated only for oxygen atoms. As mentioned above, similar mechanisms have been observed for O_3 molecules.

4.2. Dissociation of C–O bonds

The structurally important C–O bonds are found both in the disaccharides (MurNAc–GlcNAc) as well as between them. There are four oxygen atoms that are linked with two carbon neighbors in one disaccharide (see figure 1), while the other oxygen atoms in the structure have either hydrogen neighbors or they are connected with carbon atoms by double bonds. Therefore, we do not consider the breaking of these C–O bonds in this study, as they do not play a significant role in the destruction of the PG structure (see figure 1).

We observe several C–O bond-breaking mechanisms in our simulations. In all of these mechanisms, the dissociation again occurs due to the hydrogen-abstraction reaction. After the hydrogen abstraction, a double C–O bond may be formed (more specifically, one C–O bond is broken and another becomes a double bond), or a double C–C bond may be formed, or both double bonds are formed. In most cases, the hydrogen-abstraction reaction leads to a cascade of C–O bond cleavage events, i.e. the breaking of three important C–O bonds: one in MurNAc, one in GlcNAc and one between them (see figure 1). Note that here we only denote ether bonds as 'important C–O bonds', i.e., as one of two bonds between two carbon atoms and one oxygen atom in disaccharides (see figure 7(a), black dashed circles).

One of the observed consecutive breaking mechanisms of three ether bonds is presented in figure 7. Note that this mechanism is observed most in our simulation for all impinging species.

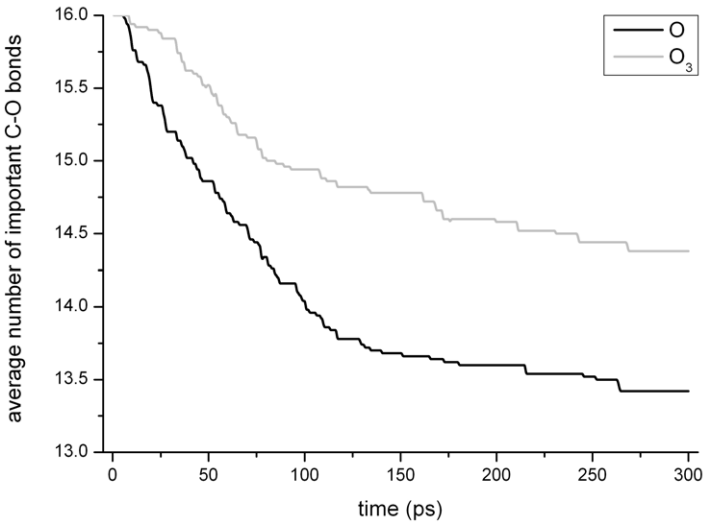

Figure 8. Time evolution of the average number of ether bonds upon the impingement of O atoms and O_3 molecules. The value of the average number is calculated from 50 simulations for each incident species.

In figure 7(a), the oxygen atom abstracts a hydrogen atom from GlcNAc with the formation of an OH radical (see first red dashed circle). After a few ps, a second oxygen atom abstracts a hydrogen atom from MurNAc and a second OH radical is formed (see figure 7(b), red dashed circle). For clarity, we numbered the atoms that participate in the dissociation of the ether bonds (see figure 7(a), black dashed circles). In figure 7(c), the OH radical abstracts another hydrogen, which is connected to C_1, with the formation of a water molecule. Consequently, a radical is created at C_1, which results in a cascade of homolytic cleavage and double bond formation reactions starting with the creation of a double C_1–O_2 bond, which in turn leads to cleavage of the C_3–O_2 bond. The latter subsequently leads to the creation of a double C_3–O_4 bond. Moreover, this leads to the cleavage of the C_5–O_4 bond, which in turn yields the formation of the double C_5–C_6 bond. This subsequently results in the dissociation of the C_6–O_7 bond and the formation of the double C_8–O_7 bond. Finally, the cascade process leads to cleavage of part of the molecule, which in turn eventually results in damage to the bacterial cell wall.

In figure 8, the time evolution of the average number of ether bonds is shown. As mentioned above, the average number of ether bonds is calculated from 50 runs for each incident species. It is clear from figure 8 that the average number decreases during the simulation, i.e. the C–O bonds are broken by the impacting plasma species. Moreover, most of the ether bond cleavage events occur due to oxygen impacts, rather than due to O_3 molecules (see figure 8). From the 50 simulations that were carried out for each type of incident species, the dissociation of the ether bonds occurs with oxygen atoms in 39 cases (i.e., 78%), whereas this value is 28 for O_3 (56% of the cases), i.e. about 1.4 times less (see table 1). We should also mention that most of the bond cleavage events occur in disaccharides, rather than in other parts of the PG structure. Thus, the dissociation of the important ether C–O bonds in disaccharides is observed much more frequently than the dissociation of C–N or C–C bonds in other parts of the PG structure. The values for C–N bond breaking are shown above and those for C–C bonds breaking are given below in section 4.3.

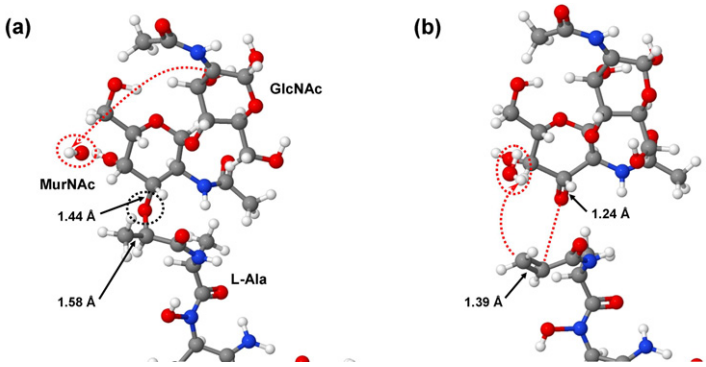

Figure 9. Snapshots from MD simulations, showing the breaking mechanism of the fourth important ether C–O bond (see black dashed circle) upon oxygen atom impact. (a) Oxygen abstracts the hydrogen atom from GlcNAc and an OH radical is formed ($t = 70.2$ ps). (b) Another hydrogen is abstracted from the methyl residue of MurNAc, which is close to the fourth ether bond, resulting in the formation of double C–C and C–O bonds, which subsequently leads to the cleavage of the fourth ether bond ($t = 70.8$ ps).

Our study on C–O bond dissociation shows that if the hydrogen-abstraction reaction is initiated at a carbon atom located near one of the three important ether bonds in disaccharides (see figure 7(a), black dashed circles), this can eventually lead to consecutive cleavage of at least two of these three C–O bonds. Moreover, we should also mention that the carbon, at which the hydrogen-abstraction reaction takes place and subsequently the dissociation of the important C–O bonds occurs, should not necessarily be a first neighbor of the participating O atom in a ring of MurNAc or GlcNAc. Indeed, the dissociation of the ether bonds in MurNAc, GlcNAc or between them can also occur when the hydrogen-abstraction reaction takes place from another carbon atom, which is the second or the third neighbor of the participating O atom in a MurNAc or GlcNAc ring. Furthermore, the cleavage of the important C–O bonds (and even cleavage of all of three) can be observed when the hydrogen abstraction takes place from a carbon or oxygen, which are positioned in the residue close to the O atom in a ring of MurNAc or GlcNAc (see figure 7(b), residues connected to C_1 and C_6).

The dissociation of a fourth ether bond occurs mostly due to the hydrogen abstraction from a methyl residue of MurNAc, which is close to this bond (see figure 9(a), black dashed circle). Indeed, after the hydrogen abstraction from the methyl residue, an unstable primary alkyl radical is created, which leads to the formation of a double C–C bond and this, subsequently, will induce the breaking of the ether bond and the formation of the double C–O bond (see figure 9(b)); the bond lengths are indicated for the sake of clarity.

It should also be mentioned that after breaking of any of the important C–O bonds in disaccharides, a double bond remains instead of two single bonds. It is also clear from figure 10 that at the beginning of the simulation, the number of single and double C–O bonds in the PG is approximately the same (see figure 10, light gray curve). However, after 150 ps, i.e. in the middle of the simulation, the number of single bonds has already decreased significantly, whereas the number of double C–O bonds has increased (see figure 10, gray curve). Finally, at the end of the simulation, the peak of the double C–O bonds becomes approximately twice as high as the

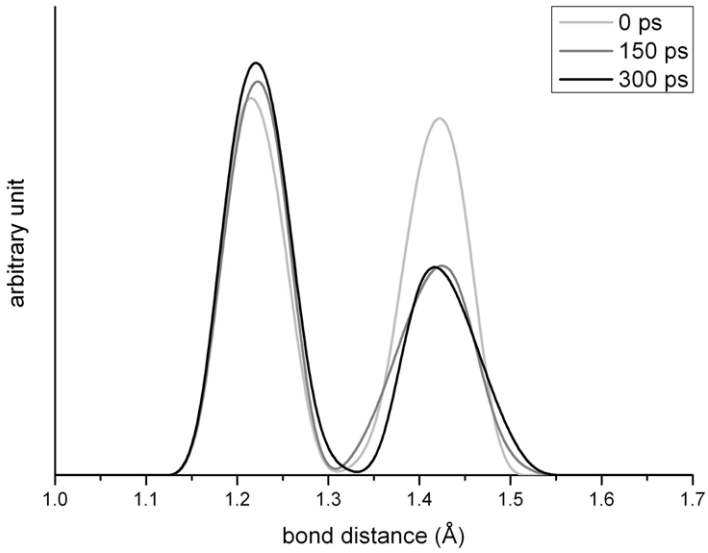

Figure 10. C–O bond length distribution after different simulation times, i.e. after 0, 150 and 300 ps. The peaks around 1.43 and 1.23 Å correspond to single and double C–O bonds, respectively.

single C–O bond peak. If we compare the maxima of the single and double C–O bond curves in the beginning and at the end of the trajectory (i.e., at 0 ps and after 300 ps, respectively), the decrease in single C–O bonds is much faster than the increase in double C–O bonds. This is due to the dissociation of single C–O bonds and formation of double C–O bonds. Indeed, the latter are formed from remaining (i.e. non-dissociated) single C–O bonds. Note that all examples of the important ether C–O bond-breaking mechanisms were shown above only for oxygen atoms. As mentioned above, similar mechanisms were observed in the case of O_3.

4.3. Dissociation of C–C bonds

As is clear from figure 1, bonds between carbon atoms are found in all parts of the PG structure. However, our investigation shows that the dissociation of C–C bonds occurs only in disaccharides and in most cases after the breaking of three ether bonds (see above).

As is the case for the C–N and the C–O bonds, a number of different bond-cleavage mechanisms are observed for C–C bond dissociation. The most frequently observed mechanism is illustrated in figure 11. In this process, the C–C bond in GlcNAc is broken after the homolytic cleavage of three ether bonds. Again, for clarity, we numbered the C atoms participating in the mechanism (see figure 11). It can be seen in figure 11(a) that after the initial hydrogen-abstraction reaction an O radical is created, which is connected to C_2. For the O radical to form a double C–O bond, one of the two C–C bonds (i.e. bonds between C_1–C_2 or C_2–C_3) needs to be homolytically broken. This bond cleavage is found to occur between C_1–C_2. This results in the formation of two molecules: one with a conjugated system (see figure 11(b), red dashed circle) and one with a resonance-stabilized radical. Note that the radical in the conjugated system is also resonance stabilized, although this radical is not important for the above-mentioned breaking mechanisms since we also observed the same mechanisms when there was no radical at that position (see figure 11, C_5).

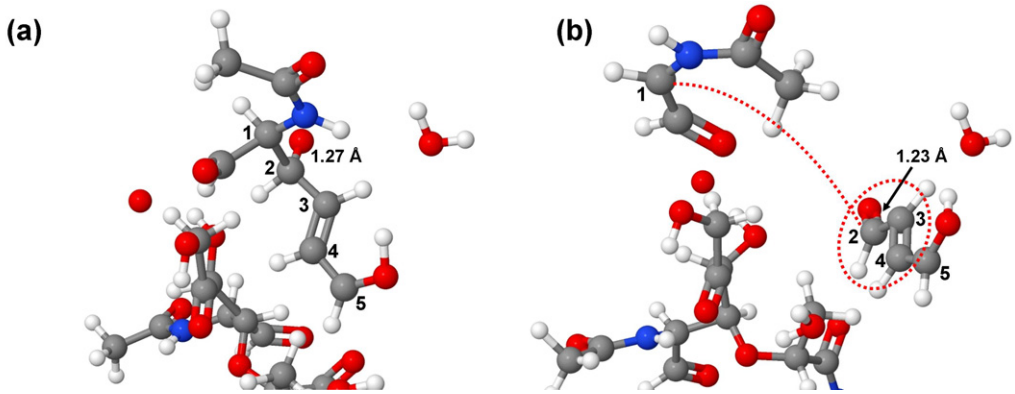

Figure 11. Snapshots from MD simulations, showing the breaking mechanism of a C–C bond upon oxygen atom impact. (a) After the hydrogen abstraction, the distance between the oxygen radical and C_2 begins to decrease ($t = 81.6$ ps). (b) Oxygen radical forms a double bond with C_2 and this leads to the cleavage of the C_1–C_2 bond ($t = 82.8$ ps). As a result, a conjugated system is formed (see red dashed circle).

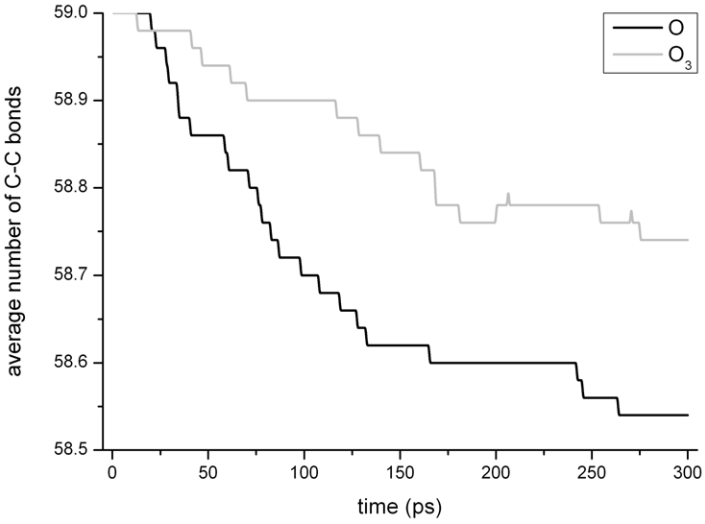

Figure 12. Time evolution of the average number of C–C bonds upon the impingement of O atoms and O_3 molecules. The value of the average number is calculated from 50 simulations for each incident species.

The time evolution of the average number of C–C bonds is depicted in figure 12. As was mentioned above, the average number of C–C bonds is calculated from 50 runs for each incident particle. It is clear from figure 12 that the average number of C–C bonds decreases during the simulation, i.e., the C–C bonds are effectively broken by impinging plasma species. Again, most of the C–C bond-breaking events occur due to oxygen impacts, rather than due to O_3 molecules. Furthermore, our investigation shows that from the 50 simulations performed for each impinging species, oxygen atoms lead to dissociation in 19 cases (38%), whereas O_3 leads to dissociation in 13 of these cases (26%, see table 1).

It should be mentioned that for O_3 molecules the same C–C bond-breaking mechanisms were observed as for the O atoms.

5. Conclusion

In this work, we investigated the interaction of important plasma species—i.e., O_3 and O_2 molecules, and O atoms—with the PG structure by means of reactive molecular dynamics simulations. We demonstrated that such atomic-scale simulations give valuable insights into the details of the microscopic events that occur in the plasma treatment of bacteria.

We found that O_2 molecules do not result in structural damage to the PG. They were found to only have weak non-bonded interactions with the PG. The other investigated plasma species, i.e., O_3 and especially O atoms, were found to break structurally important bonds of the murein (i.e. C–O, C–C and C–N bonds), which subsequently leads to structural damage of the bacterial cell wall. This is in qualitative agreement with the literature [11, 20–24], where it is indeed reported that oxygen-based active species such as atomic oxygen and ozone have a strong germicidal effect. Moreover, our atomic-level investigations revealed the important role these species play as plasma-borne disinfectants.

We found that the dissociation of C–N, C–O and C–C bonds upon O atom impacts occurred in 26, 78 and 38% of the simulation cases, respectively. Note that these percentages have been calculated from 50 simulations performed for each kind of plasma species and it is quite possible that in one simulation case impinging O atoms could give rise to the dissociation of both a C–N and a C–O bond, for instance, so the sum could be higher than 100%. For the O_3 molecules, the cleavage of C–N, C–O and C–C bonds occurred in 8, 56 and 26% of the cases, respectively. Hence, it is clear that the O atoms are more effective in bond cleavage than the O_3 molecules, and the C–O bonds seem to break up more easily, followed by the C–C bonds and C–N bonds.

The mechanisms of the important bond-breaking processes in PG were studied thoroughly. In all bond-cleavage mechanisms, the dissociation of important bonds (i.e., C–O, C–C and C–N bonds) occurs due to the hydrogen abstraction by incident particles. As mentioned above, these bonds are most frequently broken due to interaction with atomic oxygen, rather than by O_3 species. It was also found that most of the bond-breaking processes occur in disaccharides, rather than in other parts of the PG structure, i.e., the dissociation of the ether bonds in disaccharides is observed much more frequently than the dissociation of C–N or C–C bonds in other parts of the PG structure, as also mentioned above. Moreover, no bond-breaking events were observed in the pentaglycine interpeptide, even when hydrogen-abstraction reactions took place. We explain this by the resonance-stabilized structure of the pentaglycine.

C–N bond dissociations are found to occur most often in alanines, rather than in other parts of the PG structure. These dissociations are again invariably initiated by a hydrogen-abstraction reaction, removing a hydrogen atom from the methyl part of the alanines. The hydrogen-abstraction reaction which leads to the dissociation of the ether bonds in disaccharides, most often also leads to a cascade of additional ether bond-breaking events. This results in the cleavage of three important C–O bonds, i.e., the ether bonds in MurNAc and GlcNAc, and the ether bond between them. Moreover, the dissociation of a fourth important C–O bond occurs mostly due to the hydrogen abstraction from the methyl residue of MurNAc, which is close to this bond. It was also found that the cleavage of the C–C bonds occurs only in disaccharides and in most cases after the breaking of three ether bonds.

It is known that some plasma sources create higher concentrations of oxygen species than others (see e.g. [2, 21]), and they might therefore be more efficient for inactivating bacteria, since the probability of PG destruction might be higher. Our findings could therefore be useful for the development of plasma sources for enhanced antibacterial properties.

It should, however, be realized that our simulations were performed under 'perfect' conditions. In reality, bacteria are typically surrounded by a liquid film, which affects the plasma species. The effect of this liquid film has not yet been included in our study, but will be investigated in the near future. Nevertheless, we believe that our present results already provide some atomic-level insight into the mechanisms of plasma species interacting with bacteria, and in plasma disinfection in general.

Acknowledgments

This work is financially supported by the Fund for Scientific Research Flanders (FWO). This work was carried out in part using the Turing HPC infrastructure at the CalcUA core facility of the Universiteit Antwerpen, a division of the Flemish Supercomputer Center VSC, funded by the Hercules Foundation, the Flemish Government (department EWI) and the Universiteit Antwerpen.

References

[1] Kong M G, Kroesen G, Morfill G, Nosenko T, Shimizu T, van Dijk J and Zimmermann J L 2009 Plasma medicine: an introductory review *New J. Phys.* **11** 115012

[2] Ehlbeck J, Schnabel U, Polak M, Winter J, von Woedtke Th, Brandenburg R, von dem Hagen T and Weltmann K-D 2011 Low temperature atmospheric pressure plasma sources for microbial decontamination *J. Phys. D: Appl. Phys.* **44** 013002

[3] Fridman G, Friedman G, Gutsol A, Shekhter A B, Vasilets V N and Fridman A 2008 Applied plasma medicine *Plasma Process. Polym.* **5** 503–33

[4] Laroussi M, Mendis D A and Rosenberg M 2003 Plasma interaction with microbes *New J. Phys.* **5** 41

[5] Dobrynin D, Fridman G, Friedman G and Fridman A 2009 Physical and biological mechanisms of direct plasma interaction with living tissue *New J. Phys.* **11** 115020

[6] Choi J H, Han I, Baik H K, Lee M H, Han D-W, Park J-C, Lee I-S, Song K M and Lim Y S 2006 Analysis of sterilization effect by pulsed dielectric barrier discharge *J. Electrost.* **64** 17–22

[7] Babaeva N Yu, Ning N, Graves D B and Kushner M J 2012 Ion activation energy delivered to wounds by atmospheric pressure dielectric-barrier discharges: sputtering of lipid-like surfaces *J. Phys. D: Appl. Phys.* **45** 115203

[8] Laroussi M and Akan T 2007 Arc-free atmospheric pressure cold plasma jets: a review *Plasma Process. Polym.* **4** 777–88

[9] Kieft I E, v d Laan E P and Stoffels E 2004 Electrical and optical characterization of the plasma needle *New J. Phys.* **6** 149

[10] Goree J, Liu B, Drake D and Stoffels E 2006 Killing of *S. mutans* bacteria using a plasma needle at atmospheric pressure *IEEE Trans. Plasma Sci.* **34** 1317

[11] Laroussi M 2005 Low temperature plasma-based sterilization: overview and state-of-the-art *Plasma Process. Polym.* **2** 391–400

[12] Lee M H, Park B J, Jin S C, Kim D, Han I, Kim J, Hyun S O, Chung K-H and Park J-C 2009 Removal and sterilization of biofilms and planktonic bacteria by microwave-induced argon plasma at atmospheric pressure *New J. Phys.* **11** 115022

[13] Deng S, Ruan R, Mok C K, Huang G, Lin X and Chen P 2007 Inactivation of *Escherichia coli* on almonds using nonthermal plasma *J. Food Sci.* **72** M62
[14] Li Y-F, Shimizu T, Zimmermann J L and Morfill G E 2012 Cold atmospheric plasma for surface disinfection *Plasma Process. Polym.* **9** 585–9
[15] von Keudell A *et al* 2010 Inactivation of bacteria and biomolecules by low-pressure plasma discharges *Plasma Process. Polym.* **7** 327–57
[16] Lee H W, Park G Y, Seo Y S, Im Y H, Shim S B and Lee H J 2011 Modelling of atmospheric pressure plasmas for biomedical applications *J. Phys. D: Appl. Phys.* **44** 053001
[17] Zhu X M, Pu Y K, Balcon N and Boswell R 2009 Measurement of the electron density in atmospheric-pressure low-temperature argon discharges by line-ratio method of optical emission spectroscopy *J. Phys. D: Appl. Phys.* **42** 142003
[18] van Duin A C T, Dasgupta S, Lorant F and Goddard W A III 2001 ReaxFF: a reactive force field for hydrocarbons *J. Phys. Chem.* A **105** 9396–409
[19] Rahaman O, van Duin A C T, Goddard W A III and Doren D J 2011 Development of a ReaxFF reactive force field for glycine and application to solvent effect and tautomerization *J. Phys. Chem.* B **115** 249–61
[20] Laroussi M and Leipold F 2004 Evaluation of the roles of reactive species, heatUV radiation in the inactivation of bacterial cells by air plasmas at atmospheric pressure *Int. J. Mass Spectrom.* **233** 81–6
[21] Lim J-P and Uhm H S 2007 Influence of oxygen in atmospheric-pressure argon plasma jet on sterilization of *Bacillus atrophaeous* spores *Phys. Plasmas* **14** 093504
[22] Laroussi M 2009 Low-temperature plasmas for medicine? *IEEE Trans. Plasma Sci.* **37** 714
[23] Moisan M, Barbeau J, Moreau S, Pelletier J, Tabrizian M and Yahia L H 2001 Low-temperature sterilization using gas plasmas: a review of the experiments and an analysis of the inactivation mechanisms *Int. J. Pharm.* **226** 1–21
[24] Stoffels E, Sakiyama Y and Graves D B 2008 Cold atmospheric plasma: charged species and their interactions with cells and tissues *IEEE Trans. Plasma Sci.* **36** 1441–57
[25] Madhuri T K, Papatheodorou D, Tailor A, Sutton C and Butler-Manuel S 2010 First clinical experience of argon neutral plasma energy in gynaecological surgery in the UK *Gynecol. Surg.* **7** 423–5
[26] Park J T 1996 The murein sacculus *Escherichia Coli and Salmonella* ed F C Neidhardt (Washington, DC: ASM Press) pp 48–57
[27] Mengin-Lecreulx D and Lemaitre B 2005 Structure and metabolism of peptidoglycan and molecular requirements allowing its detection by the Drosophila innate immune system. *J. Endotoxin Res.* **11** 105–11
[28] Vollmer W, Blanot D and de Pedro M A 2008 Peptidoglycan structure and architecture *FEMS Microbiol. Rev.* **32** 149–67
[29] Vollmer W and Seligman S J 2010 Architecture of peptidoglycan: more data and more models *Trends Microbiol.* **18** 59–66
[30] Dmitriev B A, Toukach F V, Holst O, Rietschel E T and Ehlers S 2004 Tertiary structure of *Staphylococcus aureus* cell wall murein *J. Bacteriol.* **186** 7141–8
[31] Giesbrecht P, Kersten T, Maidhof H and Wecke J 1998 Staphylococcal cell wall: morphogenesis and fatal variations in the presence of penicillin *Microbiol. Mol. Biol. Rev.* **62** 1371–414
[32] Sharif S, Singh M, Kim S J and Schaefer J 2009 *Staphylococcus aureus* peptidoglycan tertiary structure from carbon-13 spin diffusion *J. Am. Chem. Soc.* **131** 7023–30
[33] Schneider T, Senn M M, Berger-Bächi B, Tossi A, Sahl H-G and Wiedemann I 2004 *In vitro* assembly of a complete, pentaglycine interpeptide bridge containing cell wall precursor (lipid II-Gly_5) of Staphylococcus aureus *Mol. Microbiol.* **53** 675–85
[34] Dmitriev B A, Toukach F V, Schaper K-J, Holst O, Rietschel E T and Ehlers S 2003 Tertiary structure of bacterial murein: the scaffold model *J. Bacteriol.* **185** 3458–68
[35] Vollmer W and Holtje J-V 2004 The architecture of the murein (peptidoglycan) in gram-negative bacteria: vertical scaffold or horizontal layer(s)? *J. Bacteriol.* **186** 5978–87
[36] Dmitriev B, Toukach F and Ehlers S 2005 Towards a comprehensive view of the bacterial cell wall *Trends Microbiol.* **13** 569–74

[37] Chenoweth K, van Duin A C T and Goddard W A III 2008 A ReaxFF reactive force field for molecular dynamics simulations of hydrocarbon oxidation *J. Phys. Chem.* A **112** 1040–53
[38] Neyts E C, Shibuta Y, van Duin A C T and Bogaerts A 2010 Catalyzed growth of carbon nanotube with definable chirality by hybrid molecular dynamics-force biased Monte Carlo simulations *ACS Nano* **4** 6665–72
[39] Neyts E C, van Duin A C T and Bogaerts A 2011 Changing chirality during single-walled carbon nanotube growth: a reactive molecular dynamics/Monte Carlo study *J. Am. Chem. Soc.* **133** 17225–31
[40] Valentini P, Schwartzentruber T E and Cozmuta I 2010 Molecular dynamics simulation of O_2 sticking on Pt(111) using the *ab initio* based ReaxFF reactive force field *J. Chem. Phys.* **133** 084703
[41] Mueller J E, van Duin A C T and Goddard W A III 2010 Application of the ReaxFF reactive force field to reactive dynamics of hydrocarbon chemisorption and decomposition *J. Phys. Chem.* C **114** 5675–85
[42] Fogarty J C, Aktulga H M, Grama A Y, van Duin A C T and Pandit S A 2010 A reactive molecular dynamics simulation of the silica–water interface *J. Chem. Phys.* **132** 174704
[43] Khalilov U, Neyts E C, Pourtois G and van Duin A C T 2011 Can we control the thickness of ultrathin silica layers by hyperthermal silicon oxidation at room temperature? *J. Phys. Chem.* C **115** 24839–48
[44] Khalilov U, Pourtois G, van Duin A C T and Neyts E C 2012 Self-limiting oxidation in small diameter Si nanowires *Chem. Mater.* **24** 2141–7
[45] Monti S, van Duin A C T, Kim S-Y and Barone V 2012 Exploration of the conformational and reactive dynamics of glycine and diglycine on TiO_2: computational investigations in the gas phase and in solution *J. Phys. Chem.* C **116** 5141–50
[46] Abolfath R M, van Duin A C T and Brabec T 2011 Reactive molecular dynamics study on the first steps of DNA damage by free hydroxyl radicals *J. Phys. Chem.* A **115** 11045–9
[47] Abell G C 1985 Empirical chemical pseudopotential theory of molecular and metallic bonding *Phys. Rev.* B **31** 6184–96
[48] Mortier W J, Ghosh S K and Shankar S 1986 Electronegativity-equalization method for the calculation of atomic charges in molecules *J. Am. Chem. Soc.* **108** 4315–20
[49] Janssens G O A, Baekelandt B G, Mortier W J and Schoonheydt R A 1995 Comparison of cluster and infinite crystal calculations on zeolites with the electronegativity equalization method (EEM) *J. Phys. Chem.* **99** 3251–8
[50] Berendsen H J C, Postma J P M, van Gunsteren W F, DiNola A and Haak J R 1984 Molecular dynamics with coupling to an external bath *J. Chem. Phys.* **81** 3684–90
[51] Bruice P Y 2007 *Organic Chemistry* 5th edn (Upper Saddle River, NJ: Pearson)
[52] Clayden J, Greeves N, Warren S and Wothers P 2001 *Organic Chemistry* (New York: Oxford University Press)